Met. Mater. Int., Vol. 24, No. 1 (2018), pp. 73~83
doi: 10.1007/s12540-017-7248-x

Microstructure and Mechanical Properties of Friction Stir Welded and Laser Welded High Entropy Alloy CrMnFeCoNi

Min-Gu Jo[1,2], Han-Jin Kim[1,3], Minjung Kang[2,4], Phaniraj P. Madakashira[2,*], Eun Soo Park[2], Jin-Yoo Suh[1], Dong-Ik Kim[1], Sung-Tae Hong[5], and Heung Nam Han[2,*]

[1]High Temperature Energy Materials Research Center, Korea Institute of Science and Technology, Seoul 02792, Republic of Korea
[2]Department of Materials Science and Engineering and Research Institute of Advanced Materials, Seoul National University, Seoul 08826, Republic of Korea
[3]Department of Materials Science and Engineering, Korea University, Seoul 02841, Republic of Korea
[4]Welding and Joining Research Group, Korea Institute of Industrial Technology, Incheon 21999, Republic of Korea
[5]School of Mechanical Engineering, University of Ulsan, Ulsan 44610, Republic of Korea

(received date: 11 April 2017 / accepted date: 9 May 2017)

The high entropy alloy CrMnFeCoNi has been shown to have promising structural properties. For a new alloy to be used in a structural application it should be weldable. In the present study, friction stir welding (FSW) and laser welding (LW) techniques were used to butt weld thin plates of CrMnFeCoNi. The microstructure, chemical homogeneity and mechanical behavior of the welds were characterized and compared with the base metal. The tensile stress-strain behavior of the welded specimens were reasonable when compared with that of the base metal. FSW refined the grain size in the weld region by a factor of ~14 when compared with the base metal. High-angle annular dark field transmission electron microscopy in combination with energy dispersive X-ray spectroscopy showed chemical inhomogeneity between dendritic and interdendritic regions in the fusion zone of LW. Large fluctuations in composition (up to 15 at%) did not change the crystal structure in the fusion zone. Hardness measurements were carried out in the weld cross section and discussed in view of the grain size, low angle grain boundaries and twin boundaries in FSW specimens and the dendritic microstructure in LW specimens.

Keywords: high entropy alloy, friction stir welding, laser welding, microstructure, mechanical property

1. INTRODUCTION

High entropy alloys (HEAs) contain five or more elements in equiatomic or near equiatomic composition that crystallize as a single phase [1-5]. Their design is based on the concept that high configurational entropy of mixing will stabilize the solid solution phases and preclude the formation of potentially embrittling intermetallic compounds. Research in the field of HEAs has exploded in the past ~10 years not only because of their unconventional composition but also because they often exhibit unusual physical and mechanical properties [5,6]. Although there is much to be researched with regard to the mechanisms by which the unusual properties manifest, it has been experimentally shown that the lattice is severely distorted [7,8] and that diffusion is sluggish [9] in HEAs. These two effects were suggested to have given rise to the high recrystallization temperature [10] and high resistance to grain coarsening [11].

The high entropy alloy CrMnFeCoNi containing equal amounts of chromium, manganese, iron, cobalt, and nickel, which crystallizes as the single phase face centered cubic (FCC) structure is among the more widely researched high entropy alloys [1,2,12-16]. Cantor *et al.* [2] reported the as-cast microstructure, composition in the dendritic and interdendritic regions, hardness and also the effect of adding a 6th alloying element. Their observations on microstructure and composition were reaffirmed recently in a detailed study on vacuum induction melted CrMnFeCoNi using atom probe tomography [12]. The alloy is easy to manufacture and process using conventional routes and is touted to be a promising structural material. It has a good combination of strength, ductility and fracture toughness [13,17]. Especially at lower temperatures the properties are comparable to high nickel steels and certain austenitic stainless steels [17]. Creep [14], tensile properties in the temperature range: 77-1073K, thermal stability [15], and high temperature oxidation behavior [16] of this alloy have also been investigated. Recently, Wu *et*

*Corresponding authors: mphaniraj@gmail.com, hnhan@snu.ac.kr

al. [18] investigated the weldability of this alloy using electron beam welding of 1.5 mm thick sheets. They reported that the alloy was weldable with no solidification cracks and loss in strength or ductility. However, there are no reports, to the authors' knowledge, on friction stir welding and laser welding of CrMnFeCoNi.

Laser welding (LW) [19-21] and friction stir welding (FSW) [22,23] are well established processes for joining a range of metals and alloys. It is known that in friction stir welding heat is generated by friction between tool and work-piece and by plastic deformation. The combination of heat and plastic deformation results in the occurrence of high defect densities and a mixture of recovery and recrystallization phenomena in the weld. The change in microstructure in the weld results in a change in mechanical properties across the weld [23]. In laser welding it is known that the heat source melts the material creating a fusion zone (FZ) that solidifies upon cooling and a heat affected zone (HAZ), beside FZ, which does not melt. The base metal (BM) acts as a substrate on which the new solid phase grows. The weld pool microstructure, solute segregation, hot cracking, inclusion distribution and thereby the mechanical properties depend on the solidification behavior [20]. In this paper the effect of friction stir welding and laser welding on the microstructure and mechanical properties of the welds of thin plates of CrMnFeCoNi were investigated.

2. EXPERIMENTAL PROCEDURE

Vacuum induction melting (VIM) was used to prepare 15 kg ingots of CrMnFeCoNi using equiatomic proportions of chromium, manganese, iron, cobalt, and nickel. The ingots were hot rolled at 1100 °C from 85 to 10 mm thick plates. The hot rolled plates were annealed at 1050 °C for 1 h and water quenched. The annealed plates were wire cut to make specimens for LW and FSW. The dimension of the plates for LW and FSW were 55 mm × 60 mm × 1 mm and 55 mm × 60 mm × 2 mm, respectively.

FSW (F1300, Hwacheon, Korea) of the 2 mm plates was carried out under spindle transport mode with the welding direction perpendicular to the rolling direction of the plates. The spindle was water cooled. Welds were made in a butt joint configuration. Additional HEA plates were placed on both sides of the HEA metal plates so that the FSW tool could start moving from the HEA plate on one side and stop in the HEA plate on the other side to achieve a complete weld line. The WC-12Co tool was tapered cylindrical with the dimensions: Pin diameter 4-5.76 mm, pin length 1.85 mm, shoulder diameter 12 mm and tilt angle 3°. The tool was inserted into the metal under displacement-control mode until the shoulder part made contact with the metal surface. FSW was carried at welding speed of 150 mm/min and tool rotation speeds of 600 and 700 rpm.

LW was carried out using a continuous-wave Yb:YAG disk laser (HLD 4200, TRUMPF GmbH Germany). The plates were held tight on copper back plate. Welding direction was perpendicular to the rolling direction of the plates. The laser beam, which was delivered by an optical fiber with a diameter of 200 μm, was supplied through the laser optic system with a focal length of 450 mm. The laser beam irradiated perpendicularly on the specimen at the focal position with a beam diameter of 0.6 mm. The LW parameters were chosen in order to produce a fully penetrating bead through thickness direction. Top and back side nozzles for shielding gas (argon) were used for the protection of the weld-pool. LW conditions were: 3 kW Power at welding speeds of 8 m/min and 9 m/min, 3.5 kW at 9 m/min.

Cross-weld tensile specimens were produced using wire-cutting to sub-size (ASTM E8) along the rolling direction. Tensile test was carried out (H25KT Universal testing machine, Tinius Olsen, USA) at strain rate of $8.33\times10^{-4}s^{-1}$. Four individual tests were conducted to ensure reproducibility. Fractography was carried out using scanning electron microscope (SEM: Inspect F50, FEI, USA). X-ray diffraction (XRD, D8 advance, Bruker, USA), SEM-EBSD (SEM: S-4300SE, Hitachi, Japan; EBSD: e-Flash, Bruker, USA) and transmission electron microscope (TEM, Talos F200X (super X-EDS), FEI, USA) were used to characterize the phases and microstructure of as-annealed and welded cross-sections. Specimens for EBSD were electropolished using the Struers A2 solution. To reveal the dendritic microstructure the specimens were etched in aquaregia before observing using EBSD. EBSD data was obtained at appropriate magnifications and step sizes ranging from 2.18 to 0.16 microns. The EBSD data were analyzed using the software (TSL OIM Analysis 7.3.0, EDAX, USA). The grain tolerance angle was set to 5°. The grain boundary and low angle boundary were defined as having misorientation angle greater than 15° and lower than 5°, respectively. The grain size was measured after excluding twin boundaries. Vickers hardness measurements in the weld cross-section were carried using microvickers machine (Durascan 70, EMCO, Austria). Hardness was measured under 100gf load at an interval of 400 μm.

The welded specimens that gave reasonable mechanical properties when compared with the BM were chosen for further characterization. The specimens that were FSW at 600 rpm, and LW at 3 kW at 9 m/min were characterized for microstructure and mechanical properties and presented in this paper.

3. RESULTS AND DISCUSSION

The microstructure of the BM (Fig. 1(a)) showed a number of annealing twins. The grain size, measured along normal, transverse and rolling directions, after excluding twins, was ~70 μm. The X-ray diffractogram (Fig. 1(b)) confirmed that the alloy had a single phase with FCC structure.

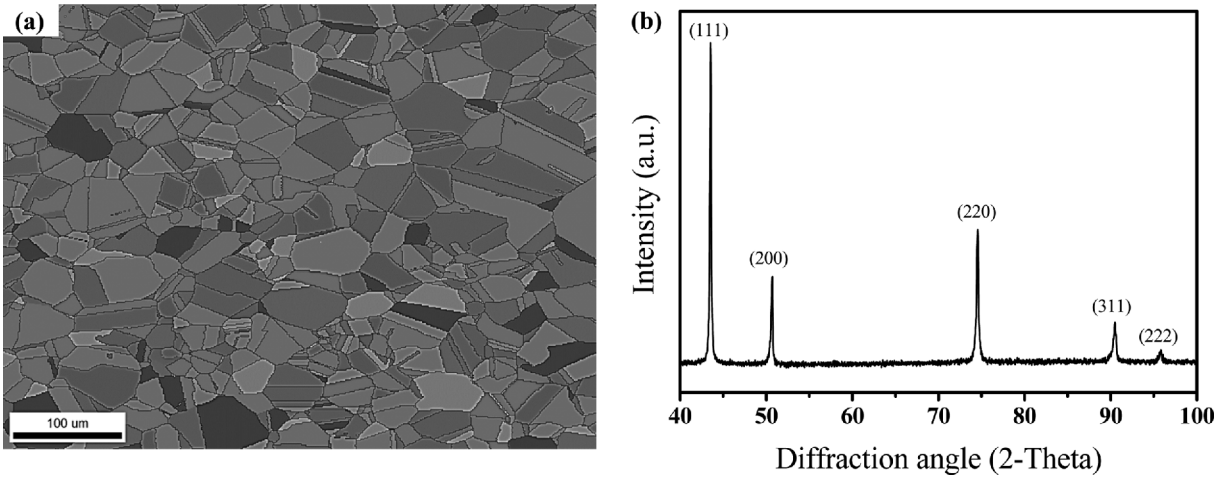

Fig. 1. Microstructure of annealed CrMnFeCoNi (a) SEM-EBSD micrograph and (b) X-ray diffractogram.

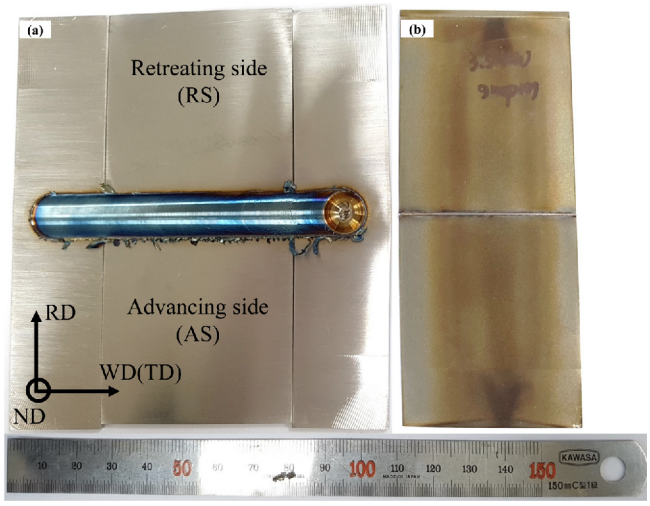

Fig. 2. Photographs of the welded specimens. (a) FSW and (b) LW.

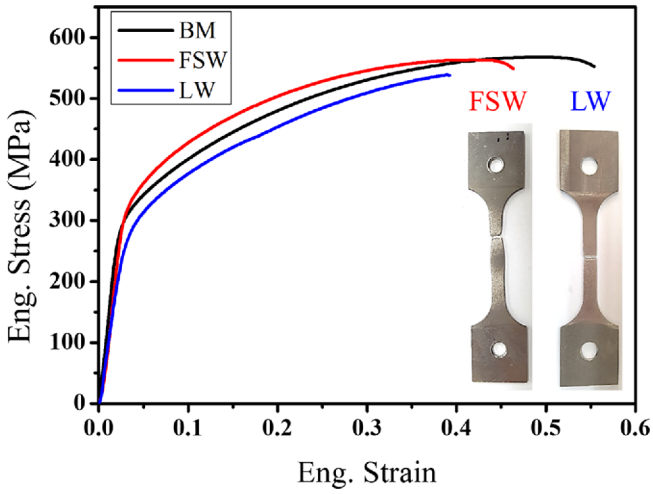

Fig. 3. Tensile stress-strain behavior of BM, FSW and LW specimens. The inset shows the welded specimens after fracture in tension test.

3.1. Stress-strain behavior

The macroscopic view of the welded specimens showed no noticeable defects. (Fig. 2). Figure 3 shows the stress-strain curves from the annealed and welded specimens. The strength and ductility of the welded specimens were comparable with that of the BM. The FSW specimen had relatively higher yield strength (296 MPa) when compared with that of the base metal (272 MPa). The loss in ductility in the FSW specimen (9%) was less than that in the LW specimen (16%). The tensile fracture occurred in the BM away from the weld center in the FSW specimen whereas in the LW specimen fracture occurred in the weld center i.e. in the FZ (see inset in Fig. 3). The fracture surface in both FSW and LW specimens showed features of dimpled rupture, which is typical of ductile fracture (Fig. 4). The dimples were finer in LW specimen when compared with those in the FSW specimen.

It is important note here that the tensile properties reported above are from cross-weld specimens. Therefore, the gauge length in FSW specimens contained at least three different characteristic microstructures: the base metal, thermomechanically affected zone and the stir zone. Each of these zones have different deformation resistance because of their different microstructure. To determine tensile properties of each zone tensile specimens from each zone need to be tested. Such a study was reported, see for instance, Ref. [24] for austenitic stainless steels and also noted in the review on FSW of aluminum and other metallic alloys Ref. [25]. The stacking fault energy of the CrMnFeCoNi is comparable to that of low stacking fault energy (SFE) austenitic stainless steels and make a good comparison with the present study. The high weld hardness and low ductility reported [24] in FSW cross-weld specimens of low SFE austenitic stainless steels support our observations.

Similarly, the gauge length in LW specimens contained the base metal, heat affected zone and fusion zone, each with a

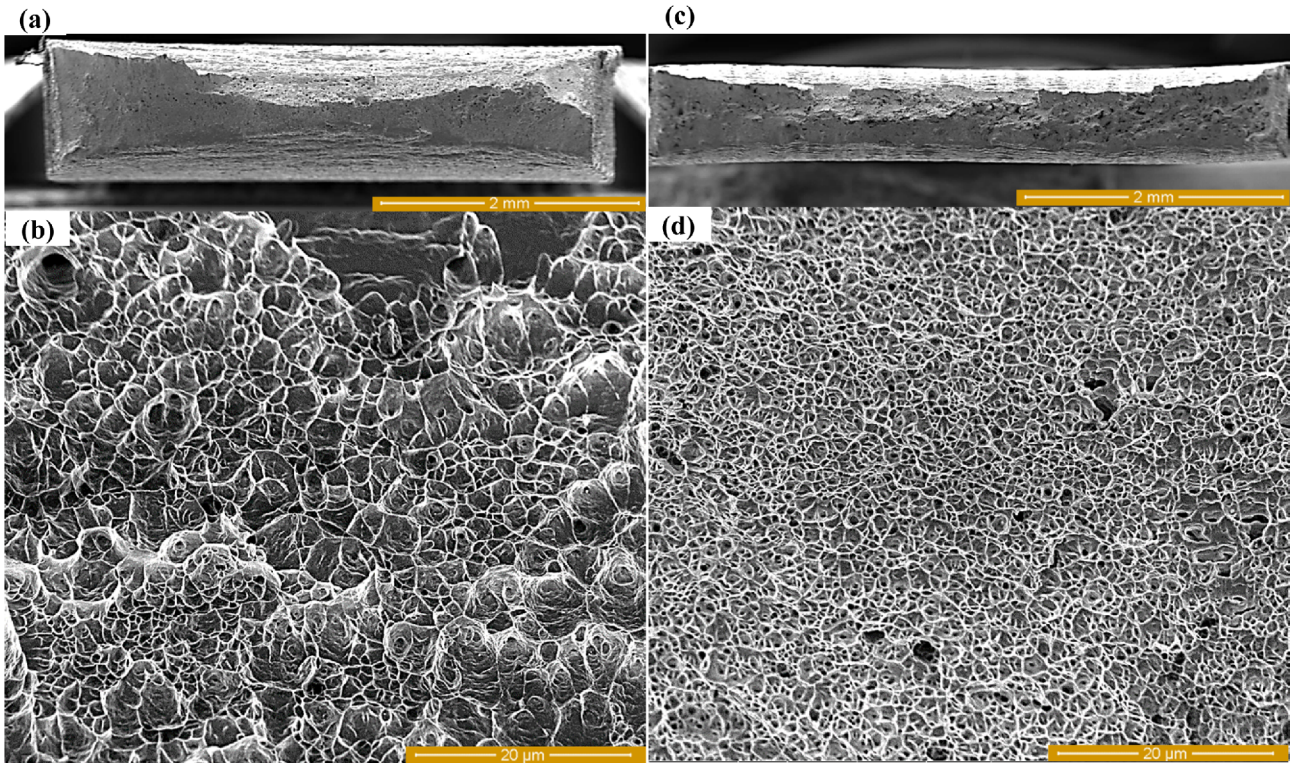

Fig. 4. Overview and detailed view of the fracture surface of welded specimens. (a, b) FSW and (c, d) LW

different microstructure. Thereby, the tensile properties of cross-weld LW specimens were the average response of these microstructures to deformation and cannot be attributed to a local microstructure. However, it is possible to generalize that fracture will occur in the weakest region of the weld [25]. The fracture of the FSW specimen in the base metal and not in the weld region indicates that the microstructure in the weld region was much finer and thereby stronger than the base metal as will be evident from section 3.2.1. The relatively higher yield strength of the FSW specimen also indicates a finer weld microstructure and therefore stronger weld region. The fracture of the LW specimen was due to oxide inclusions in the fusion zone as will be discussed in section 3.2.2. Similarly, the presence of long columnar dendrites (see Fig. 9(a) and section 3.2.2), in the fusion zone of LW specimen were possibly the reason for its relatively lower yield strength.

3.2. Weld microstructure and hardness

3.2.1. Friction stir weld

3.2.1.1. Microstructure

Figure 5(a) shows the collage of micrographs from the cross-section of weld and (b) SEM-EBSD inverse pole figure (IPF) maps from different locations along the center line in the weld cross-section. It can be seen that the microstructure on both sides of the weld center extending from -2 mm to 2 mm was significantly refined. The grain size was measured at the respective locations denoted in the cross-section in Fig. 5 and plotted in Fig. 6. The grain size in the weld center was lower than that in the BM by a factor of ~14 viz. from ~70 μm in the BM to 5 μm. The grain refinement indicates that dynamic recrystallization occurred during FSW. This is in agreement with Komarasamy *et al.* [26] who reported that friction stir processed Al0.1CoCrFeNi HEA recrystallized dynamically resulting in fine grain size. Figure 7 shows the fraction of low angle grain boundaries (LAGBs) and twin boundaries at different locations along the center of the weld. The fraction of LAGBs is highest at the center and decreases with increasing distance away from the weld center. The twin boundary fraction decreases with increasing distance from the BM to the region at the weld center.

During FSW, the material beneath the tool experiences thermomechanical effects. The temperature due to friction and deformation under the tool pin can rise to 80%-90% of the melting point (T_m), for e.g. peak temperature was $0.8T_m$ during FSW of 304 stainless steel [27,28]. Dynamic recrystallization is the mechanism of accommodating deformation during thermomechanical processing in low stacking fault energy metals. The static recrystallization temperature of CrMnFeCoNi was reported to be high at $0.62T_m$ [10]. Thereby in view of the high temperature generated during FSW and the relatively low stacking fault energy viz. 17-27 mJ/m^2 [29] of CrMnFeCoNi, grain refinement in the weld region due to dynamic recrystal-

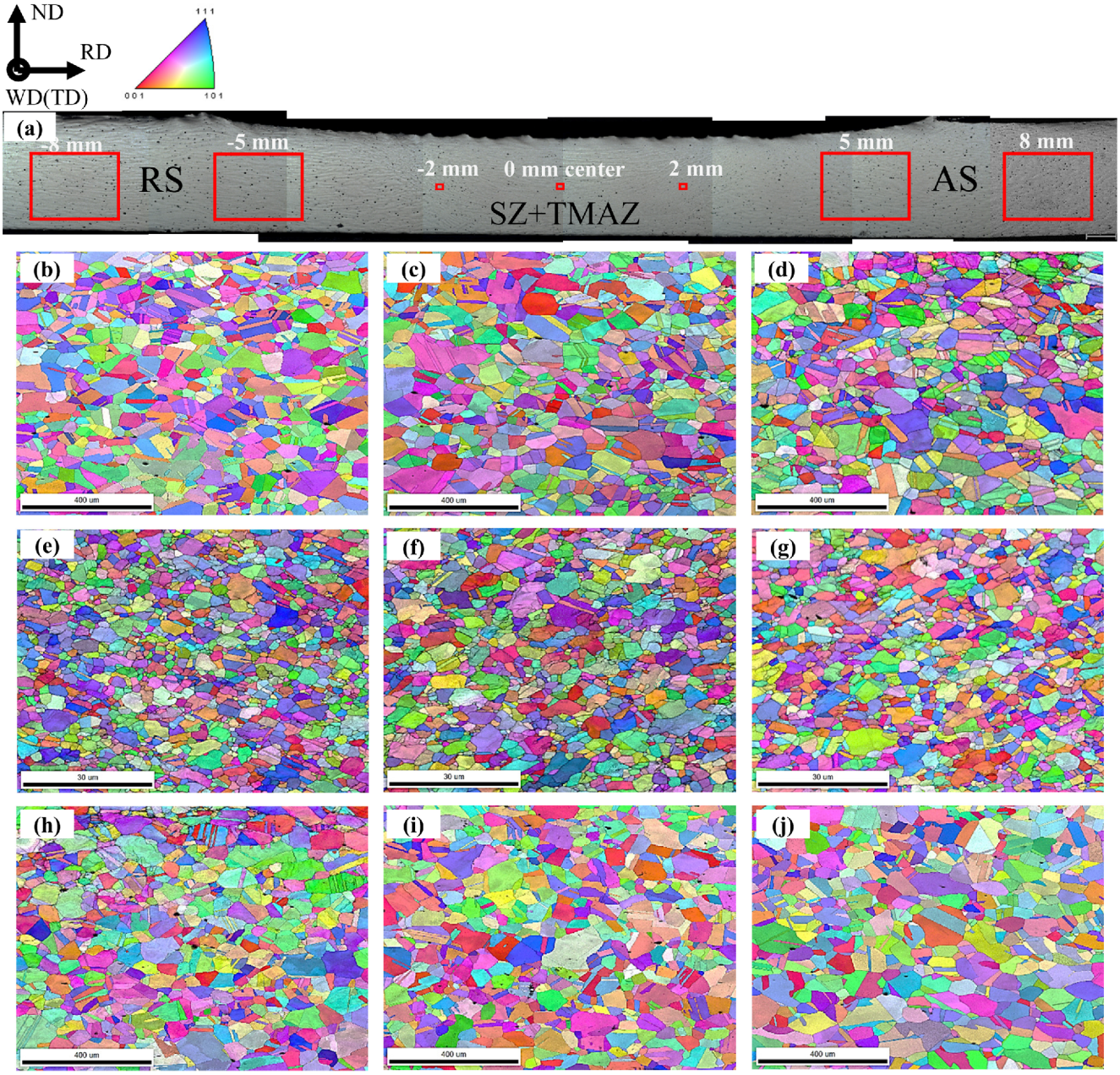

Fig. 5. (a) Collage of optical micrographs from the cross-section of the FSW specimen. The red boxes indicate weld center and at 2 mm, 5 mm, 8 mm, 10 mm from the weld center where SEM-EBSD was carried out to obtain the optical micrographs below (b-j). Advancing side (AS), Retreating (RS), Stir zone (SZ) thermo-mechanically affected zone (TMAZ).

lization was possible. During FSW, the tool rotates and moves along the welding direction so the welded area heats up quickly and cools giving less time for recrystallization and grain growth (in the present study welding time is < 25 s). In addition, CrMnFeCoNi is unusually resistant to coarsening. In cold worked and recrystallized CrMnFeCoNi grain coarsening does not set in up until 800 °C [10]. The fine grain size in the weld region is maintained despite the high temperature generated during FSW because of the high grain coarsening temperature and the relatively less time that the welded area is exposed to high temperatures. The latter is one reason for the relatively high fraction of LAGBs and the decrease in twin boundary fraction in the weld region. Bhattacharjee *et al.* [10] also have reported LAGBs in deformed and annealed CrMnFeCoNi. They speculated that dislocation energy would be lower in a severely distorted lattice, thereby making it difficult to eliminate dislocations during recrystallization. However, further study is needed to understand these effects.

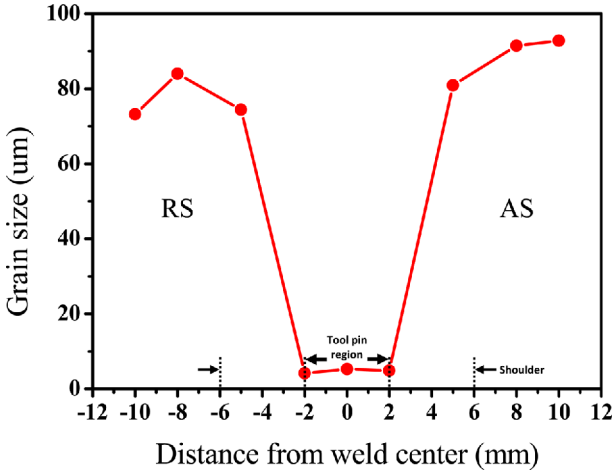

Fig. 6. Grain size at different distances from weld center positions shown in Fig. 5.

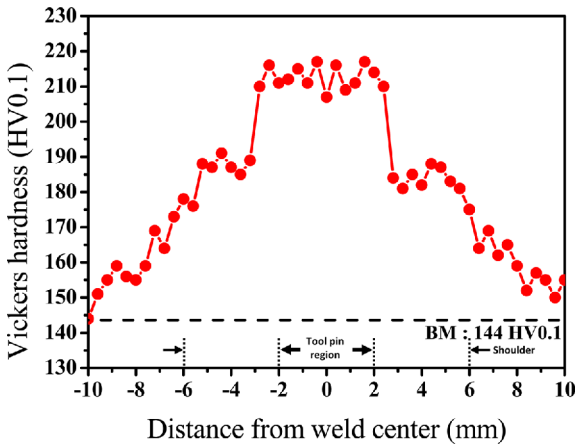

Fig. 8. Vickers hardness in the weld cross-section at 400 μm intervals in the weld cross-section of the FSW specimen.

3.2.1.2. Hardness

The hardness of the BM was 144 HV. Figure 8 shows the hardness measured in the weld cross-section at 400 μm intervals. It can be seen that the hardness is much higher than the BM in the weld region and there is no significant difference between advancing and retreating sides. The tool pin region, marked in Fig. 8, had relatively higher hardness than the region under the tool shoulder. The hardness decreases steadily to that of the BM at the periphery of the tool shoulder region. The higher hardness in the tool pin region is commensurate with the ~14 times finer grain size in this region. The presence of LAGBs (Fig. 7(a)) in this region also indicates that the material was still in the deformed condition, which also contributed to the high hardness of this region.

3.2.2. Laser weld

3.2.2.1. Microstructure

Figure 9(a) shows the SEM-EBSD micrographs (IPF maps) of the cross-section of the LW. There were no macro or micro cracks in the FZ or in the region beside the FZ i.e., the HAZ. The FZ gives the appearance of a columnar grained microstructure with random crystallographic orientation. Each of these grains consist of dendrites (see Fig. 9(b)) that grew from the grains in the FZ-BM boundary to the weld centerline, as discussed below. Figure 9(c) shows the higher magnification EBSD micrograph from the region containing the FZ-BM i.e. the dotted square overlaid in Fig. 9(a). Typically in the LW the HAZ manifests in the form of change in microstructure, for e.g. grain size, relatively to the BM. However, no significant change

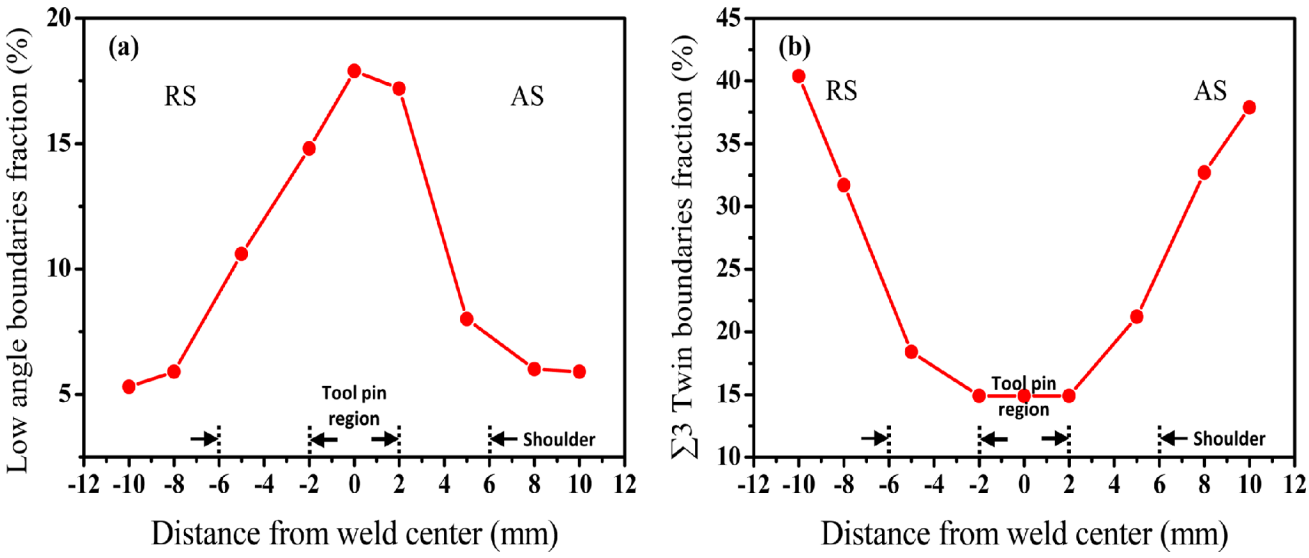

Fig. 7. (a) Low angle grain boundaries fraction and (b) Twin boundaries fraction at different distances from weld center.

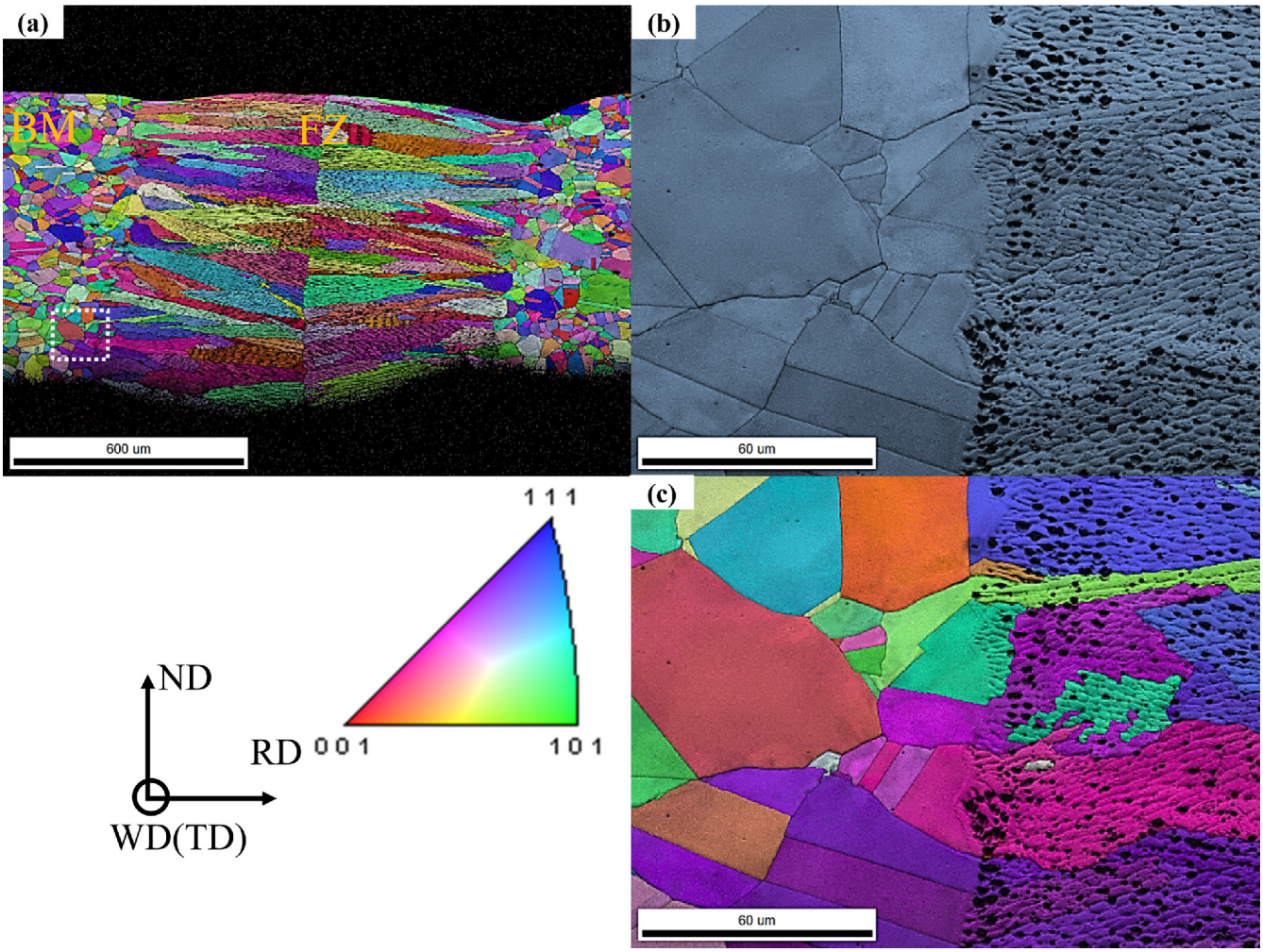

Fig. 9. (a) EBSD micrograph (IPF map) of the cross-section of the LW specimen showing the FZ and the BM. (b) detailed EBSD micrograph (Phase map) and (c) (IPF map) from the square region marked in white dots in (a).

in microstructure near the FZ-BM boundary was observed in the present study. Figure 10 shows a high magnification IPF map from the FZ-BM boundary. The yellow square marked in Fig. 10(a) was chosen for measuring composition fluctuation across dendrites. EDS line scan across the dendrites showed that the interdendrite regions were relatively rich in manganese whereas the dendrites themselves were relatively rich in iron (see Fig. 10(b)). The enrichment of Fe in the dendrite and Mn in the interdendrite region is in agreement with the reports of Cantor *et al.* [2] and Laurent-Brocq *et al.* [12] on the same alloy in the induction melted and cast condition.

Figure 11 shows the STEM-HAADF micrograph with EDS-element maps and line scan from the center of the FZ. It is evident from the maps and the line scan across the specimen that the composition is not homogeneous. The interdendritic and dendritic regions are enriched in manganese and iron, respectively, similar to that at the FZ-BM boundary (Fig. 10(b)). The EDS-line scan also shows that in general the dendrites were also enriched in iron and depleted in nickel and manganese. The fluctuation in composition is significant viz. between ~5 and 15 at%. The cause for this compositional fluctuation in the FZ, which is expected to stay hot longer than the FZ-BM boundary and thereby allow for greater homogenization, is not clear and needs further study. The relatively dark spherical particles evident in the HAADF image and all the element maps (marked by arrows in Mn-map) were found to be rich in manganese, sulfur and oxygen indicating that these were manganese sulfides/oxides. Figure 12 shows HADDF image and element maps of two such particles. These inclusions form inevitably during initial ingot manufacture and during melt solidification in the FZ. Inclusions are known to be detrimental to ductility [30] and were among the reasons for the relatively lower ductility in the LW specimen.

In order to verify if the fluctuation in composition caused a

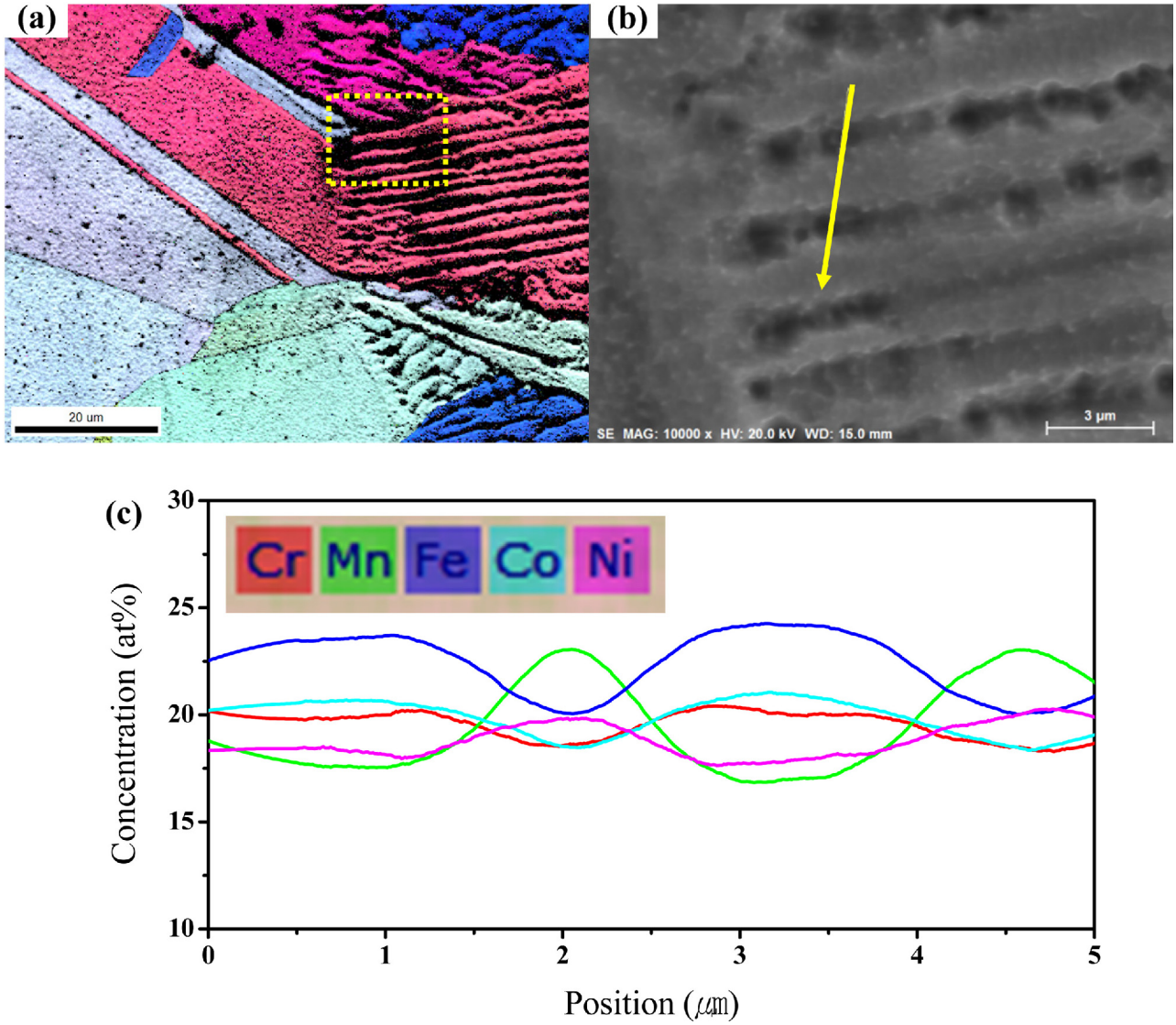

Fig. 10. (a) EBSD micrograph (IPF map) from the FZ-BM boundary showing dendrites emerging from the BM grains. (b) SEM micrograph and the yellow line across which the EDS line scan was conducted. (c) EDS line scan across the region marked in yellow in (b).

change in phase structure electron diffraction was carried out in the FZ (Fig. 13). It can be seen from the diffraction patterns in Fig. 13 that the Mn-rich and Fe-rich regions have the FCC structure. This indicates that the structure of CrMnFeCoNi is stable and not affected by large fluctuations in composition.

3.2.2.2. Hardness

The hardness in the weld cross-section is shown in Fig. 14. The hardness in the FZ was higher than the BM. Hardness in dendritic microstructures is typically related to the dendrite arm spacing (DAS). Cast microstructures with finer DAS are known to have higher hardness [31]. The primary DAS in the FZ was at least of the order ~1 μm (see Fig. 10(b)) which is considerably finer when compared with the relatively coarse grained BM and could be one of the reasons for the higher hardness. Schuh *et al.* [31] reported that that hardness increase and consequent loss in ductility upon annealing severely deformed CrMnFeCoNi was because of the formation of nanoscale phases embedded in the HEA matrix making it like a composite. In the present study, the presence of fine regions alternately rich in manganese and nickel or chromium, iron and cobalt in the HEA matrix give it the nature of a composite. Cantor *et al.* [2] correlated the local change in composition between dendritic and interdendritic regions with 3%-4% change in hardness. In view of the above reports[2,32], it is possible that the hardness increase and hardness fluctuation observed in the present study is

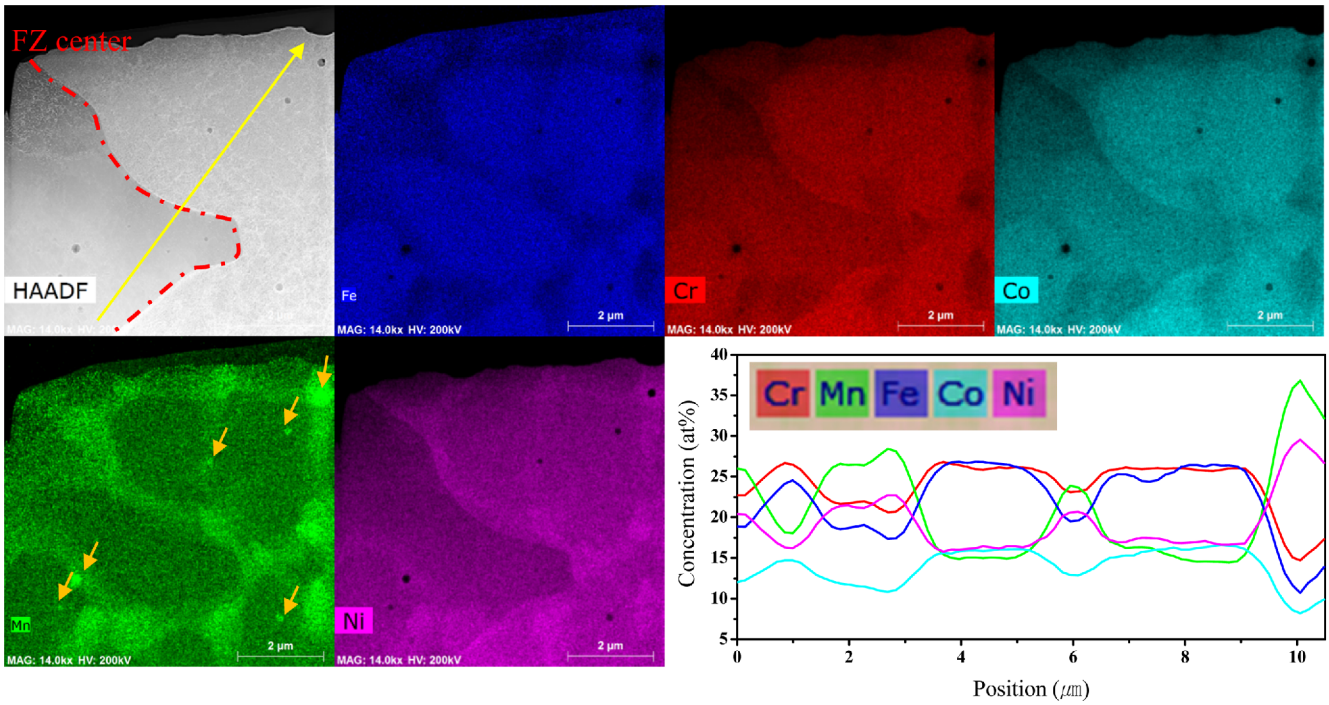

Fig. 11. STEM-HAADF micrograph and element maps at the center of the FZ. The EDS line scan was conducted along the yellow line marked in the HAADF image. The arrows in the Mn-map indicate the oxide/sulfide inclusions characterized in Fig. 12.

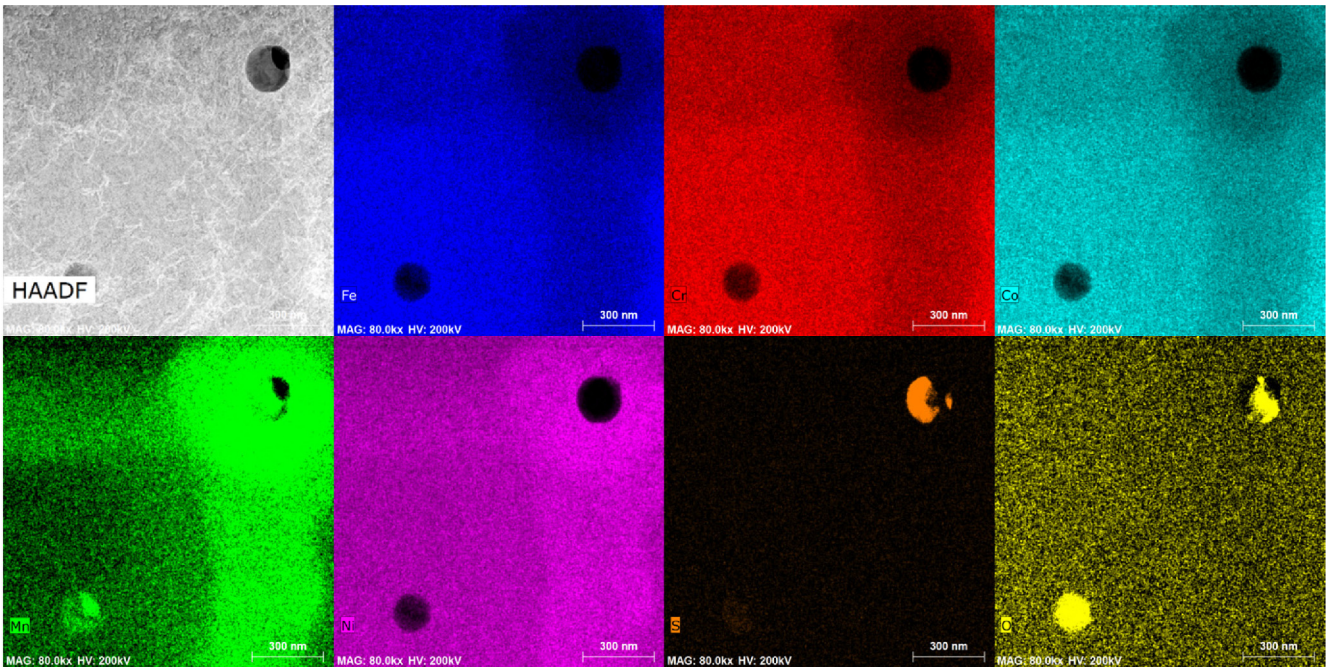

Fig. 12. STEM-HAADF micrograph and element maps at the center of the FZ showing that the areas marked by arrow in the Mn-map in Fig. 11 are rich in oxygen and sulfur.

possibly due to the local changes in composition (Fig. 10(b)) particularly in the FZ (see Fig.11) with large composition fluctuations. However, further investigation is needed to verify the hardness-composition dependence and will be the subject of future study.

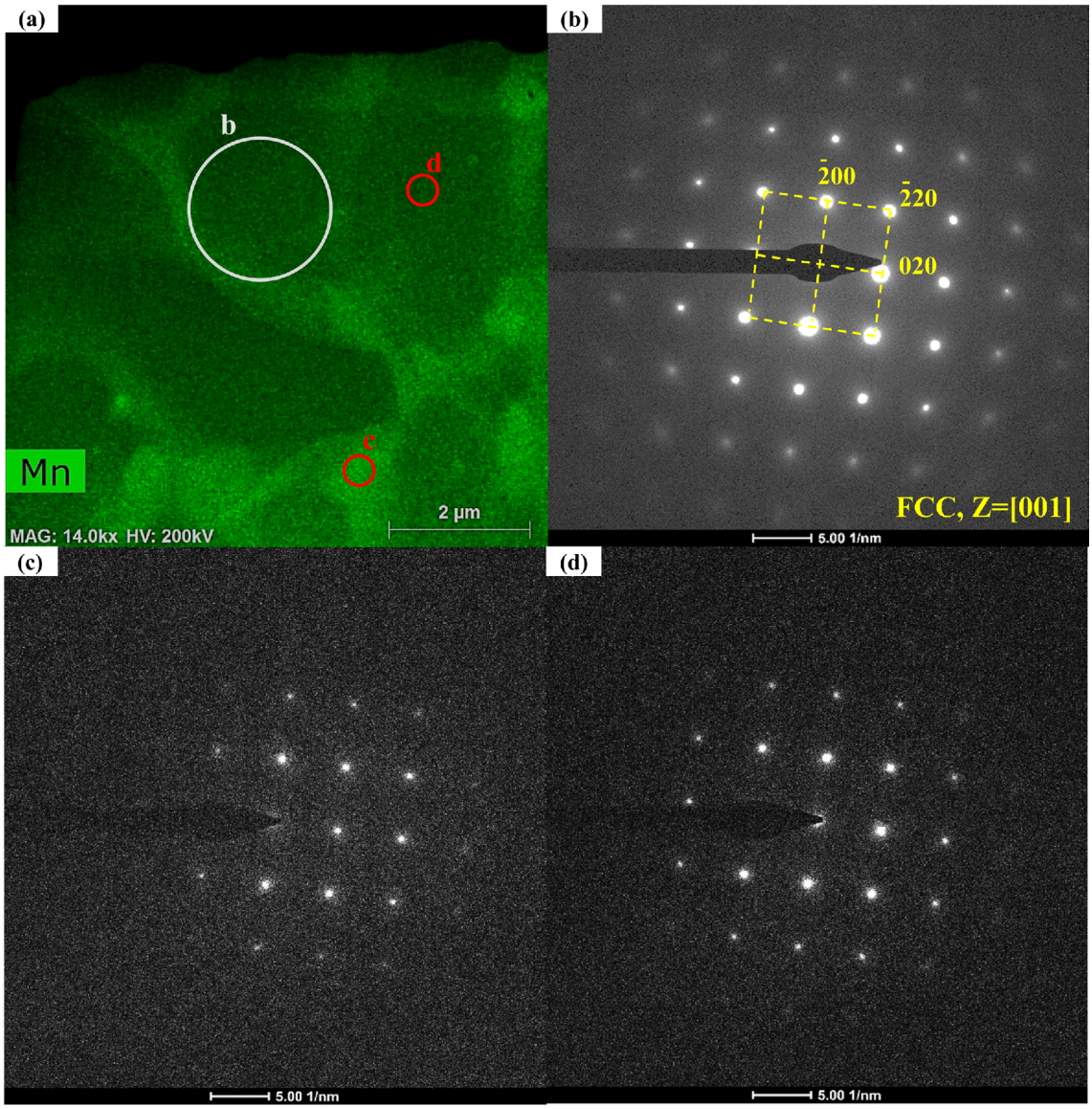

Fig. 13. (a) Mn-map from Fig. 11 and electron diffraction patterns from areas marked (b) frame, (c) Mn-rich area and (d) Fe-rich region

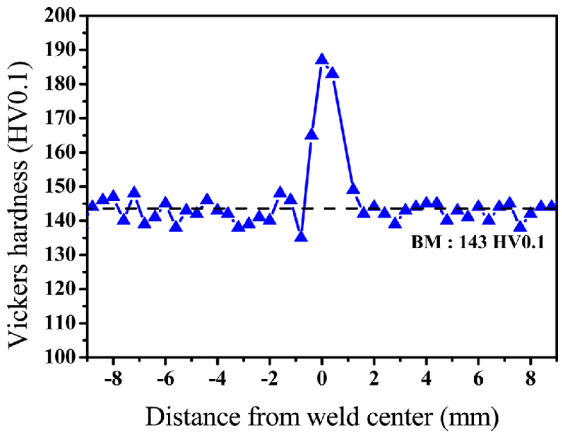

Fig. 14. Vickers hardness at 400 μm intervals in the weld cross-section of the LW specimen.

4. CONCLUSION

1 mm and 2 mm thick plates of the high entropy alloy CrMnFeCoNi were welded using FSW and LW, respectively. The welded specimens were characterized for their microstructure and mechanical properties.

(1) The tensile strength and ductility of FSW and LW CrMnFeCoNi were comparable to that of annealed CrMnFeCoNi. The FSW specimens had better tensile strength and ductility than LW specimens. The relatively lower ductility of the LW specimen was partly due to manganese oxide/sulfide inclusions in the FZ.

(2) Dynamic recrystallization during FSW reduced the grain size by a factor of 14 when compared with the BM. This was proposed to be due to the high recrystallization tempera-

ture, high resistance to grain growth of the alloy and short duration of welding.

(3) The FZ in the LW specimens had a dendritic structure. In general the dendritic and interdendritic regions were relatively rich in iron and manganese, respectively. The relatively large composition inhomogeneity in the center of the FZ did not affect the crystal structure. No other phases or intermetallic compounds formed in the weld.

(4) Hardness of the FSW specimen was higher than the BM because of the finer grain size and high fraction of LAGBs. LW specimens had higher hardness than the BM because of the fine dendrite arm spacing and possibly because composition fluctuations in the HEA matrix gave it a composite nature.

ACKNOWLEDGEMENT

This work was supported by the Engineering Research Center (ERC) program of the National Research Foundation of Korea (NRF) grant funded by the Ministry of Science, ICT & Future Planning (MSIP) (NO. NRF-2015R1A5A1037627). The work at Korea Institute of Science and Technology (KIST) was supported by the Convergence Agenda Program (CAP) of the Korea Research Council of Fundamental Science and Technology.

REFERENCES

1. J.-W. Yeh, S.-K. Chen, S.-J. Lin, J.-Y. Gan, T.-S. Chin, S.-Y. Chang, *et al*. *Adv. Eng. Mater.* **6**, 299 (2004).
2. B. Cantor, I. T. H. Chang, P. Knight, and A. J. B. Vincent, *Mat. Sci. Eng. A* **375**, 213 (2004).
3. M. C. Gao, J.-W. Yeh, P. K. Liaw, and Y. Zhang, *High Entropy Alloys: Fundamentals and Applications*, p. 8, Springer International, Switzerland (2016).
4. E. J. Pickering and N. G. Jones, *Int. Mater. Rev.* **61**, 183 (2016).
5. B. S. Murty, J.-W. Yeh, and S. Ranganathan, *High-Entropy Alloys*, p. 13, Butterworth-Heinemann, UK (2014).
6. J.-W. Yeh, *JOM* **65**, 1759 (2013).
7. J.-W. Yeh, S.-Y. Chang, Y.-D. Hong, S.-K. Chen, and S.-J. Lin, *Mater. Chem. Phys.* **103**, 41 (2007).
8. Y. Zhang, Y. J. Zhou, J. P. Lin, G. L. Chen, and P. K. Liaw, *Adv. Eng. Mater.* **10**, 534 (2008).
9. K.-Y. Tsai, M.-H. Tsai, and J.-W. Yeh, *Acta Mater.* **61**, 4887 (2013).
10. P. P. Bhattacharjee, G. D. Sathiaraj, M. Zaid, J. R. Gatti, C. Lee, J.-W. Yeh, *et al. J. Alloy. Compd.* **587**, 544 (2014).
11. W. H. Liu, Y. Wu, J. Y. He, T. G. Nieh, and Z. P. Lu, *Scripta Mater.* **68**, 526 (2013).
12. M. Laurent-Brocq, A. Akhatova, L. Perrière, S. Chebini, X. Sauvage, Y. Champion, *et al. Acta Mater.* **88**, 355 (2015).
13. F. Otto, A. Dlouhy, C. Somsen, H. Bei, G. Eggeler, and E. P. George, *Acta Mater.* **61**, 5743 (2013).
14. J. Y. He, C. Zhu, D. Q. Zhou, W. H. Liu, T. G. Nieh, and Z. P. Lu, *Intermetallics* **55**, 9 (2014).
15. E. J. Pickering, R. Munoz-Moreno, H. J. Stone, and N. G. Jones, *Scripta Mater.* **113**, 106 (2016).
16. W. Kai, C. C. Li, F. P. Cheng, K. P. Chu, R. T. Huang, J. J. Kai, *et al. Corros. Sci.* **108**, 209 (2016).
17. B. Gludovatz, A. Hohenwarter, D. Catoor, E. H. Chang, E. P. George, and R. O. Ritchie, *Science* **345**, 1153 (2014).
18. Z. Wu, S. A. David, Z. Feng, and H. Bei, *Scripta Mater.* **124**, 81 (2016).
19. D. L. Olson, T. A. Siewert, S. Liu, and G. R. Edwards, *ASM handbook: Welding, Brazing, and Soldering*, p. 49, ASM International, USA (1993).
20. S. A. David and J. M. Vitek, *Int. Mater. Rev.* **34**, 213 (1989).
21. S. A. David, S. S. Babu, and J. M. Vitek, *JOM* **55**, 14 (2003).
22. W. M. Thomas, E. D. Nicholas, J. C. Needham, M. G. Murch, P. Temple-Smith, and C. J. Dawes, *International Patent Application PCT/GB92/02203 and GB Patent Application 9125978.8*, UK Patent Office, UK (1991).
23. R. Nandan, T. DebRoy, and H. K. D. H. Bhadeshia, *Prog. Mater. Sci.* **53**, 980 (2008).
24. E. Almanza-Casas, M. J. Perez-López, R. Steel, and S. Packer, *Proc. The Twenty-first International Offshore and Polar Engineering Conference*, p. 530, International Society of Offshore and Polar Engineers, USA (2011).
25. R. S. Mishra and Z. Y. Ma, *Mater. Sci. Eng. R-Rep.* **50**, 1 (2005).
26. M. Komarasamy, N. Kumar, Z. Tang, R. S. Mishra, and P. K. Liaw, *Mater. Res. Lett.* **3**, 30 (2015).
27. S. Pal and M. P. Phaniraj, *J. Mater. Process. Tech.* **222**, 280 (2015).
28. K. Okamoto, S. Hirano, M. Inagaki, S. H. C. Park, Y. S. Sato, C. D. Sorensen, *et al. Proc. The Fourth International Symposium on Friction Stir Welding*, p. 14, The Welding Institute, USA (2003).
29. A. J. Zaddach, C. Niu, C. C. Koch, and D. L. Irving, *JOM* **65**, 1780 (2013).
30. H. K. D. H. Bhadeshia and R. W. K. Honeycombe, *Steels: Microstructure and Properties*, p. 239, Butterworth-Heinemann, UK (2006).
31. M. C. Flemings, *Metall. Trans.* **5**, 2121 (1974).
32. B. Schuh, F. Mendez-Martin, B. Völker, E. P. George, H. Clemens, A. Hohenwarter, *et al. Acta Mater.* **96**, 258 (2015).